2D Zn-Porphyrin-Based Co(II)-MOF with 2-Methylimidazole Sitting Axially on the Paddle–Wheel Units: An Efficient Electrochemiluminescence Bioassay for SARS-CoV-2

Yi-xuan Li, Jing Li, Dunru Zhu, Ju-zheng Wang, Sheng-li Zhang, Xue-ji Zhang, Guo-fang Shu, Junji Li, Serge Cosnier, Hai-bo Zeng, et al.

2D Zn-porphyrin-based Co(II)-MOF with 2-Methylimidazole Sitting Axially on the Paddle-wheel Units: An Efficient Electrochemiluminescence Bioassay for SARS-CoV-2

Yi-Xuan Li, Jing Li, Dunru Zhu, Ju-Zheng Wang, Guo-Fang Shu, Junji Li, Sheng-Li Zhang*, Xue-Ji Zhang, Serge Cosnier, Hai-Bo Zeng, Dan Shan**

Y. Li, J. Li, J. Wang, Dr. J. Li, S. Zhang, X. Zhang, H. Zeng, D. Shan
MIIT Key Laboratory of Advanced Display Materials and Devices
School of Environmental and Biological Engineering
Nanjing University of Science and Technology
Nanjing 210094, P R China
E-mail: danshan@njust.edu.cn; zhangslvip@njust.edu.cn

D. Zhu
State Key Laboratory of Materials-Oriented Chemical Engineering
College of Chemical Engineering
Nanjing Tech University
Nanjing 211816, P R China
E-mail: zhudr@njtech.edu.cn

G. Shu
Department of Clinical Laboratory; School of Medicine
Zhongda Hospital; Southeast University
Nanjing 210009, P R China

X. Zhang
School of Biomedical Engineering, Health Science Centre
Shenzhen University
Shenzhen 518060, P R China

S. Cosnier
University of Grenoble Alpes-CNRS
DCM UMR 5250
F-38000 Grenoble, France

Keywords: porphyrin, heterobimetallic 2D MOF, axial coordination, ECL probe, SARS-CoV-2

Abstract: High electrocatalytic activity with tunable luminescence is crucial for the development of electrochemiluminescence (ECL) luminophores. In this work, a porphyrin-based heterobimetallic 2D MOF, [(ZnTCPP)Co_2(MeIm)] (**1**), has been successfully self-assembled from the zinc(II) tetrakis(4-carboxyphenyl)porphine (ZnTCPP) linker and cobalt(II) ions in the presence of 2-methylimidazole (MeIm) by a facile one-pot reaction in methanol at room temperature. On the basis of the experimental results and the theoretical calculations, the MOF **1** contains paddle-wheel [$Co_2(-CO_2)_4$] secondary building units (SBUs) axially coordinated by a MeIm ligand, which is very beneficial to the electron transfer between the Co(II) ions and oxygen. Combining the photosensitizers ZnTCPP and the electroactive [$Co_2(-CO_2)_4$] SBUs, the 2D MOF **1** possesses an excellent ECL performance, and can be used as a novel ECL probe for rapid non-amplified detection of the RdRp gene of SARS-CoV-2 with an extremely low limit of detection (~30 aM).

1. Introduction

Electrochemiluminescence (ECL) is an electrochemically triggered chemiluminescence reaction where excited states are generated by electron transfer between reactive intermediates and radicals produced by redox of luminophores or coreactants.[1] In general, the luminescent efficiency can be greatly improved by attaching the coreactants to the ECL system.[2] However, due to the molecular diffusion in the solution, the electron transfer between coreactants and luminophores is ineffective, rendering great limitations for the enhancement of ECL intensity.[3] Therefore, the integration of the coreactant's accelerators and luminophores can serve as an effective ECL amplification strategy, which can improve the generation and collision efficiency of active intermediates originated from coreactants and luminophores.[4]

Recently, metal-organic frameworks (MOFs) materials have emerged as strong contenders for enhanced ECL luminophores owing to the facile tunability of metal ions and organic ligands, large surface areas and abundant open metal sites.[5] Among the reported systems, porphyrin-based two-dimensional (2D) MOFs were considered as ideal candidates for enhanced ECL performances based on the following advantages: (1) the porphyrin itself is a luminophore because of its large conjugated ring; (2) the porphyrin ring decorated with

coordinated groups can act as a suitable ligand for constructing 2D MOFs; (3) both the metal ion in the center of porphyrin ring and the metal ions in the MOFs can be judiciously selected for building homo- or hetero-bimetallic 2D materials; (4) the rich open metal sites in the 2D MOFs could be used to finely regulate the ECL properties without affecting the structure of the network. Up to now, two porphyrin-based homobimetallic 2D MOFs, $[Zn_2(ZnTCPP)]\cdot 3H_2O\cdot 2DEF$ and $[Co_2(CoTCPP)]\cdot 2H_2O\cdot 4.75DMF$ (ZnTCPP = zinc(II) tetrakis(4-carboxyphenyl)porphine; DEF = *N*,*N*′-diethylformamide; DMF = *N*,*N*′-dimethylformamide), have been reported.[6] However, the construction of the porphyrin-based heterobimetallic 2D MOFs remains a big challenge.

Herein, a novel porphyrin-based heterobimetallic 2D MOF, $[(ZnTCPP)Co_2(MeIm)]$ (**1**), has been successfully designed and synthesized from the self-assembly of ZnTCPP and Co(II) salts in the presence of 2-methylimidazole (MeIm) at room temperature **(Scheme 1)**. MOF **1** has been fully characterized by ultraviolet-visible spectroscopy (UV-vis), Fourier transform infrared (FT-IR), powder X-ray diffraction (PXRD), scanning electron microscopy (SEM), transmission electron microscopy (TEM), X-ray photoelectron spectroscopy (XPS), thermogravimetric analysis (TGA), electron paramagnetic resonance (EPR) spectrum and fluorescence spectroscopy.

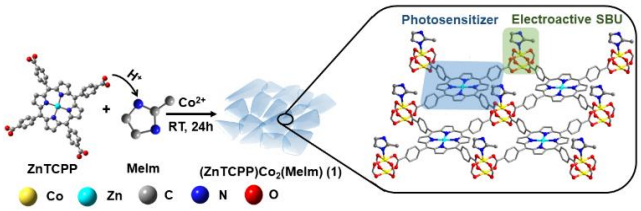

Scheme 1. Design and construction of MOF **1**.

MOF **1** possesses well-known paddle-wheel $[Co_2(-CO_2)_4]$ secondary building units (SBUs) which are also a kind of electroactive modules. Combining the photosensitizers ZnTCPP and the electroactive $[Co_2(-CO_2)_4]$ SBUs, MOF **1** can serve as an important "two in one" platform for efficient ECL amplification. Notably, the MeIm ligand axially coordinated on the paddle-wheel $[Co_2(-CO_2)_4]$ SBUs is beneficial to the electron transfer between the low-spin Co(II) ions and oxygen. Consequently, oxygen anionic radicals ($O_2^{\bullet-}$) can be efficaciously produced by the electroactive $[Co_2(-CO_2)_4]$ modules. In addition, the axially coordinated MeIm ligand can also adjust the 2D MOF **1** to a suitable distance of layers without changing the structure of layer for easy entry of O_2 and enough exposure of ZnTCPP. Integration of the sufficient exposure of photosensitizers ZnTCPP and the efficient generation of $O_2^{\bullet-}$ via the electroactive $[Co_2(-CO_2)_4]$ SBUs in a single platform synergistically enhances the ECL performance of

MOF **1**. Compared with the 2D MOF [Co_2(ZnTCPP)] (**2**) without MeIm ligand which was also prepared by us for control experiments, the MOF **1** exhibits 3.4 times higher ECL intensity than that of MOF **2**. The MOF **1** with an excellent ECL performance has been applied as a novel ECL probe for rapid non-amplified detection of the RdRp gene of SARS-CoV-2 with an extremely low limit of detection (LOD) of ~30 aM. Furthermore, the ECL probe shows an excellent sensitivity and stability, which will expect to liberate the detection of SARS-CoV-2 from the burdensome polymerase chain reaction (PCR) amplification method.

2. Results and Discussion

2.1. Synthesis and characterization of MOF 1

MOF **1** was prepared by mixing ZnTCPP with MeIm, followed by addition of Co(II) salt. In the FT-IR spectrum of MOF **1**, the $\nu_{as}(COO^-)$ and $\nu_s(COO^-)$ vibrations are separated by 152 cm^{-1}, suggesting the bidentate bridging coordination of the carboxylate group **(Figure S1A)**.[7] In the solid-state UV-vis spectrum an additional absorption in the range of 420-475 nm is observed, which corresponds to the *d-d* transition of six-coordinated Co(III) **(Figure S1B)**.[8] The XRD patterns of MOFs **1** and **2** in the (110) plane are consistent with those simulated from the reported homobimetallic 2D MOFs [Zn_2(ZnTCPP)] and [Co_2(CoTCPP)] **(Figure 1A)**.[6] Therefore, we believe that MOF **1** maintains the 2D structure assembled from ZnTCPP and paddle-wheel [$Co_2(\text{-}CO_2)_4$] SBUs. The changes of the other XRD peaks may ascribe to the variable distance of layers in the *c*-direction due to the axial coordination of MeIm on the paddle-wheel [$Co_2(\text{-}CO_2)_4$] SBUs. Thus, the introduction of MeIm is expected to adjust MOF **1** to a suitable layer spacing without changing the layer structure, which is beneficial to the entrance of O_2 and the exposure of ZnTCPP. The TEM **(Figure 1B and S3)** and SEM images **(Figure S2)** show that the average size of the MOF **1** is 200 nm, which is reduced compared with the MOF **2** without MeIm. The smaller particle size of the MOF **1** could be attributed to the accelerated nucleation during the self-assembly of Co(II) salts and the deprotonated ZnTCPP with the help of MeIm. The uniform nanostructure is beneficial to the exposure of the photosensitive ZnTCPP units in the MOF **1** to oxygen radicals.

The existence of MeIm in MOF **1** was evidenced by TGA **(Figure 1C)**. Compared with the two weight loss processes of MOF **2** (loss of the substituents on porphyrin ring and collapse of the porphyrin skeleton),[9] MOF **1** shows an additional weight loss (6.2%) during 270-384 ^oC due to the removal of MeIm (calcd. 7.8%).[10] Considering that the decomposition temperature of MeIm in MOF **1** is higher than that (198 ^oC) of free MeIm, we can reasonably

speculate that the MeIm in MOF **1** is coordinated to Co(II) ions, rather than merely physically encapsulated.

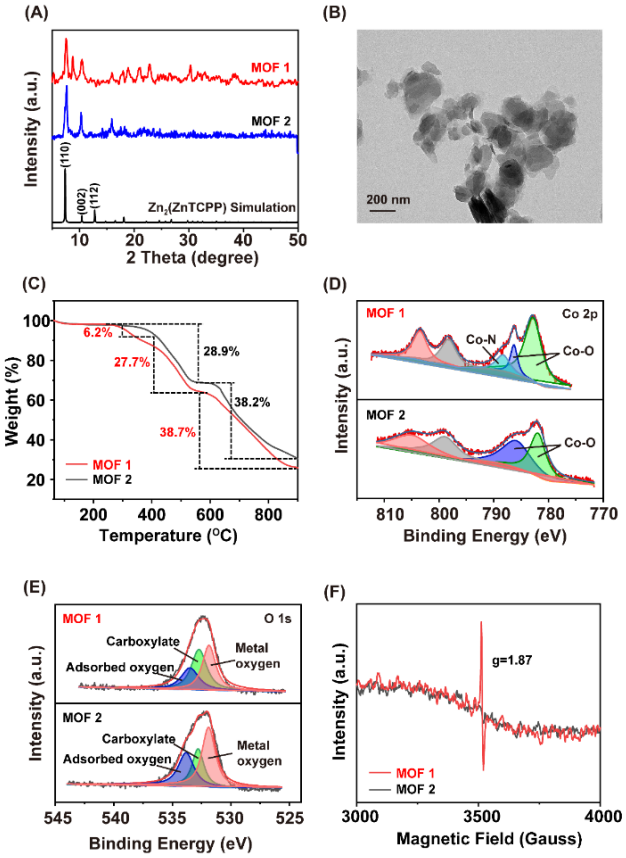

Figure 1. (A) XRD patterns of MOFs **1** and **2**. (B) HRTEM images of MOF **1**. (C) TGA of MOFs **1** and **2**. High-resolution XPS of (D) Co 2p region and (E) O 1s region of MOFs **1** and **2**. (F) EPR spectra of MOFs **1** and **2**.

Then coordination mode of the MeIm to Co(II) ions is further investigated. In the XPS spectra of MOF **1**, the Co 2p3/2 region displays an additional characteristic peak of Co-N bond at 788.0 eV **(Figure 1D)**,[11] implying that MeIm acts as an axial ligand to sit on the paddle-wheel [$Co_2(\text{-}CO_2)_4$] SBUs, as also confirmed in the N 1s region **(Figure S4)**.[12] The decreased peak for adsorbed oxygen in O 1s region of MOF **1** suggests that the water or methanol solvents on the open Co(II) sites are obviously reduced in contrast to MOF **2** **(Figure 1E)**,[13] revealing that MeIm and solvents are competing for axial coordination to Co(II) ions. Compared to MOF **2**, the EPR spectrum of MOF **1** displays a characteristic signal at 1.87 **(Figure 1F)**, exhibiting that the Co(II) ions in MOF **1** are five-coordinate in a low-spin state ($t_{2g}^6 e_g^1$, S = 1/2) and MeIm is axial coordinated on the paddle-wheel [$Co_2(\text{-}CO_2)_4$] SBUs.[14] Manipulating the electronic structures of Co(II) ions is expected to increase its

binding activity for oxygen and stimulate electron transfer to generate metal-bound superoxide (M-$O_2^{\bullet-}$).[15]

2.1. Effect of the axial coordinated MeIm

Then we finely tuned the amount of axial coordinated MeIm on paddle-wheel [$Co_2(-CO_2)_4$] SBUs and investigated the effect on electrochemical activity. XRD patterns were used to monitor the results from the different amounts. When the amount of MeIm reaches 0.04 mmol (ZnTCPP:MeIm = 1:4), a new diffraction peak appears at 2θ = 5.24° **(Figure S6)**, which is due to the axial coordinated MeIm increasing the distance of layers in **1** along the *c* axis. When MeIm is 0.06 mmol (ZnTCPP:MeIm = 1:6), the diffraction peak shifted to 2θ = 5.20°, indicating that both the axial positions of paddle-wheel [$Co_2(-CO_2)_4$] SBUs are occupied by MeIm ligands, thereby further increasing the interplanar distance in the *c*-direction **(Figure S7)**. The changes of XRD patterns prove that the numbers of axial coordinated MeIm can adjust the interlayer distance of 2D MOF **1**, making the entrance of O_2 easier and exposure of ZnTCPP more sufficient **(Figure S8)**. Furthermore, the effect of axial coordinated MeIm numbers on the electrochemical activity was investigated. **Figure 2A** shows the cyclic voltammetry (CV) curves of different modified electrodes under O_2-saturated conditions. Regardless of the presence of MeIm, all samples exhibit a reduction activity towards O_2 **(Figure S9)**. However, when MeIm is axially coordinated on the paddle-wheel [$Co_2(-CO_2)_4$] SBUs, a clear cathodic shift in the formal redox potential is observed, suggesting that the axial coordination of electron-donating MeIm ligand can not only increase the electron density around Co(II) catalytic site, but also decrease the barrier of electron transfer to form the metal-bound superoxide (Co-$O_2^{\bullet-}$). Consequently, increasing the amounts of MeIm from 0 to 0.05 mmol, the ECL intensity of MOF **1** is enhanced about 3.4 times **(Figure 2B)**. However, the catalytic and ECL performance of MOF **1** decline sharply when the amount of MeIm is equal to 0.06 mmol (ZnTCPP: MeIm = 1:6), because if the concentration of MeIm is too high, both the axial positions of the paddle-wheel [$Co_2(-CO_2)_4$] SBUs will be occupied by MeIm ligands so that there is no open metal sites available for combining oxygen. Therefore, the optimal amount of MeIm used for the synthesis of MOF **1** is 0.05 mmol (ZnTCPP:MeIm = 1:5). Under the optimal condition, MOF **1** exhibits an enhanced and stable ECL performance, which is much stronger than those of the homobimetallic MOFs, [(ZnTCPP)Zn_2(MeIm)] and [(CoTCPP)Co_2(MeIm)] **(Figure S10 and S11)**. The poor ECL performance of [(CoTCPP)Co_2(MeIm)] is due to the single electron in the e_g orbital in Co(II) quenching the ECL spectra when it acts as the central metal of the porphyrin ring. On the other hand, [(ZnTCPP)Zn_2(MeIm)] shows poor catalytic activity towards oxygen, resulting in its ECL

strength is only 17.6% of MOF **1**. The decent ECL performance of MOF **1** can be ascribed to the following four reasons: (1) The axially coordinated MeIm ligand can adjust the 2D MOF **1** to a suitable distance of layers, making O_2 more accessible and ZnTCPP more fully exposed; (2) The $[Co_2(\text{-}CO_2)_4]$ SBU with an axially coordinated MeIm, as an electroactive site, shows a higher affinity and catalytic activity for O_2; (3) MOF **1** under an oxygen-containing environment can promote electron transfer of the low-spin Co(II) ion ($t_{2g}^6e_g^1$) to O_2; (4) The ordered arrangement of the electroactive $[Co_2(\text{-}CO_2)_4]$ SBUs and the photosensitizers (ZnTCPP) effectively shortens the distance between $O_2^{\bullet-}$ and porphyrin rings and accelerates the collision of free radicals.

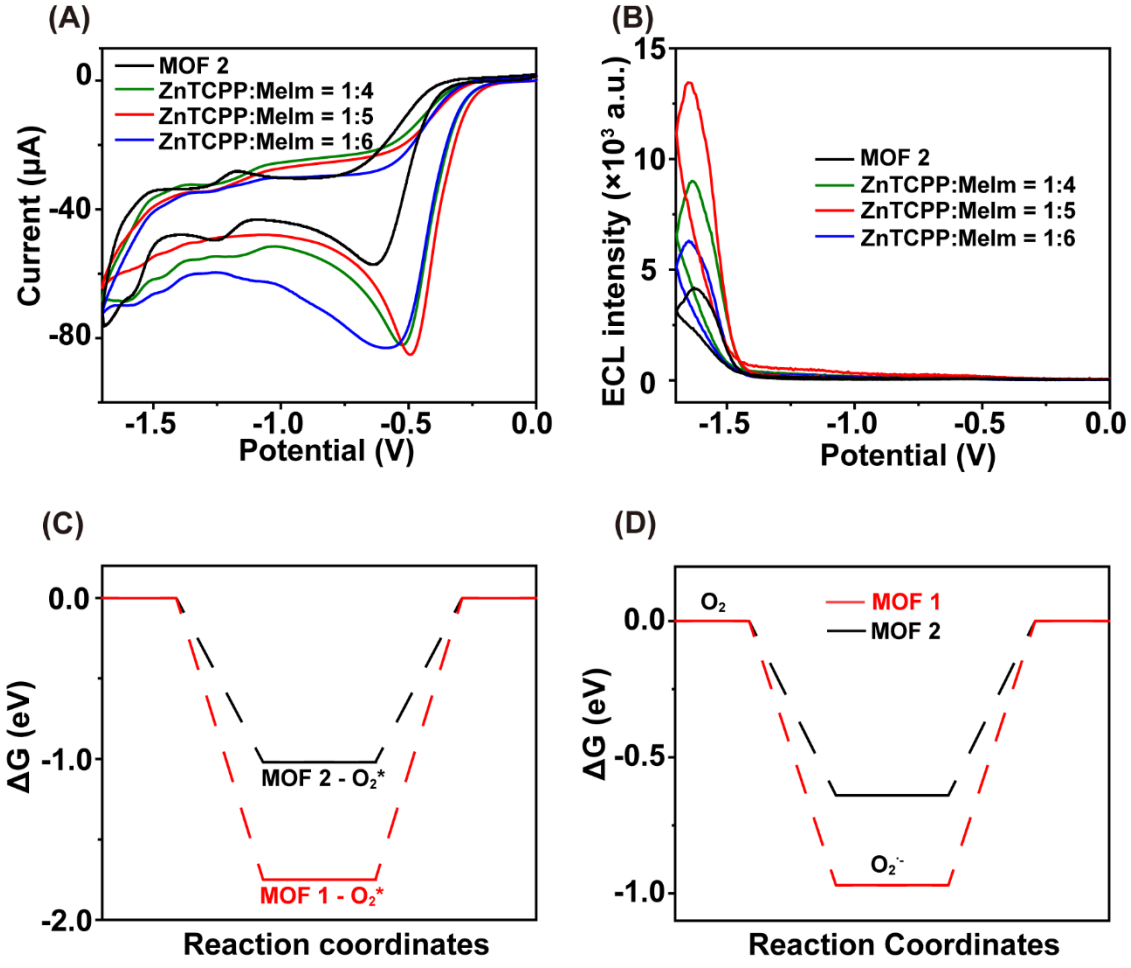

Figure 2. (A) Cyclic voltamograms of MOFs **1** and **2** with different concentrations of MeIm in 10 mmol L^{-1} HEPES (pH 7.4) containing 0.3 mol L^{-1} O_2-saturated KCl solution vs Ag/AgCl reference potential. (B) ECL-potential curves of MOFs **1** and **2** with different concentrations of MeIm in aqueous solution under O_2-saturated condition. (C) Free-energy diagram of O_2 adsorption on active Co(II) sites in MOFs **1** and **2**. (D) The free energy profile for the reduction of oxygen to $O_2^{\bullet-}$ pathway over MOFs **1** and **2**.

To further understand the role of $[Co_2(\text{-}CO_2)_4]$ SBU with an axially coordinated MeIm in activating oxygen, density functional theory (DFT) calculations were performed to investigate the Gibbs free energies and electronic distributions of MOF **1** with different amounts of MeIm during the reaction. The adsorbed O_2 is bound to the $[Co_2(\text{-}CO_2)_4]$ SBU in the form of Co-O-O. If there is only one axially coordinated MeIm on the $[Co_2(\text{-}CO_2)_4]$ SBU, both the adsorption energy (E_{ads}) of O_2 and the energy required to form $O_2^{\bullet-}$ in MOF **1** are lower than those in MOF **2**, which explains the higher electroreductive activity of O_2 in MOF **1 (Figure 2C and 2D)**. However, if there are two axially coordinated MeIm ligands on the $[Co_2(\text{-}CO_2)_4]$ SBU, it is impossible for oxygen to be adsorbed on the Co(II) ions owing to lack of open metal sites, which accounts for the decreased catalytic activity of O_2 when the amounts of MeIm reaches 0.06 mmol. Additionally, the desorption energy of $O_2^{\bullet-}$ in MOF **1** is smaller than that in MOF **2 (Figure S12)**, indicating that the $O_2^{\bullet-}$ species generated in MOF **1** are more likely to be desorbed and collide with the porphyrin anion radicals to produce $^1O_2$ intermediates.

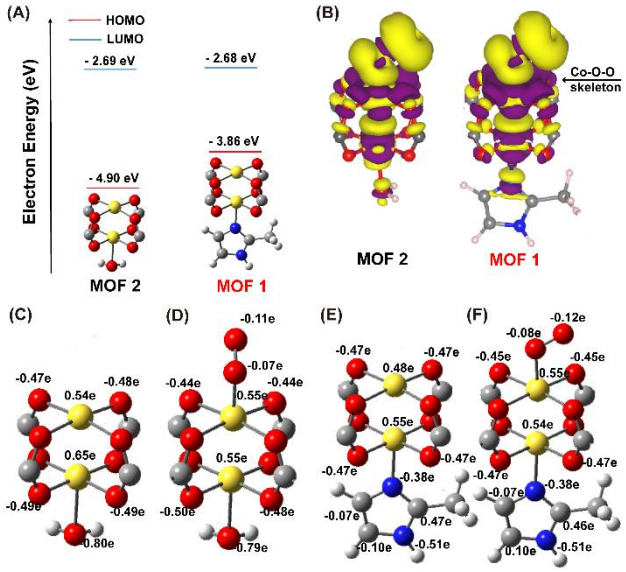

Figure 3. (A) Schematic diagrams of energy level distributions of HOMO and LUMO for MOFs **1** and **2**. (B) The charge difference distributions of MOFs **1** and **2** after oxygen binding obtained by DFT calculation, the isosurfaces are set to 0.001 e bohr^{-3} (Yellow, charge accumulation; Purple, charge depletion). Mulliken charge distributions of MOF **2** (C, D) and MOF **1** (E, F) before and after oxygen binding.

To further study the above process, the electron transfer between Co(II) ion and oxygen in MOF **1** was investigated. MOF **1** has a higher HOMO energy level than MOF **2**

($HOMO_{MOF\ 1}$= -3.86 eV, $HOMO_{MOF\ 2}$ = -4.90 eV), which shows that the Co(II) ion in MOF **1** is easier to transfer electron to O_2 **(Figure 3A)**. According to the charge distribution analysis **(Figure 3B)**, the charge density over the Co-O-O skeleton within MOF **1** is higher than that of MOF **2**. Based on the charge difference of absorbed O_2, it can be seen that the O-O bond is more likely to be broken in MOF **1**.[16] On the basis of the Mulliken charge, more intuitive data can be obtained. After binding oxygen, the positive charge of the Co(II) ion in MOF **1** changes from 0.48 to 0.55e **(Figure 3E and 3F)**, which means the Co(II) ion loses 0.07e (only 0.01e in MOF **2**, **Figure 3C and 3D**), proving that the electron transfer path of [Co^{2+}-O_2 → Co^{3+}-$O_2^{\bullet-}$] is more possible to occur in MOF **1**. This inference can also be confirmed by the results from the XPS spectra of Co 2p (Figure 1D), which reveal that the proportion of Co^{3+} in MOF **1** is higher than that in MOF **2** (Co^{3+}/Co^{2+} = 5.26 and 0.88 for MOF **1** and **2**, respectively; Co^{3+}: 782.8 eV, Co^{2+}: 786.3 eV). By the way, MOF **1** in an oxygen-containing environment can also promote electron transfer of the low-spin Co(II) ion ($t_{2g}^6 e_g^1$) to O_2.

2.2. ECL amplification mechanism

To gain more insight into the mechanism of ECL amplification, the ECL and photoluminescence (PL) spectra of MOF **1** were measured. In contrast to the typical porphyrin PL peaks located at 610 and 660 nm, the ECL emission peak of MOF **1** locates around 634 nm, which is consistent with the emission band of $^1O_2$ **(Figure S14B)**[18]. To elucidate further which kind of intermediates is involved in the ECL amplification, we introduced benzoquinone (quencher of $O_2^{\bullet-}$)[17] and NaN_3 (quencher of $^1O_2$),[18] respectively, into the ECL system. The results revealed that the ECL intensity is remarkably reduced in the presence of both 10 mM benzoquinone and NaN_3 **(Figure S15)**. In the EPR spectra **(Figure 4A)**, 12 hyperfine splitting peaks (corresponding to the superimposed spectra of $HOO^{\bullet}$ and $O_2^{\bullet-}$) are captured at the O_2 reduction potential (-0.6 V), while a group of three congruous Zeeman splits ($^1O_2$-entrapped signal) is observed at the emission potential (-1.6 V).[18] Based on the EPR analysis and ECL quenching study, we believe that O_2 is first reduced to $HOO^{\bullet}$ and $O_2^{\bullet-}$ **(Figure S16)**, which is the basis of the ECL reaction. Subsequently, the porphyrin is gradually reduced to anionic radical ($ZnTCPP^{\bullet-}$) and acted as a photosensitizer to produce $^1O_2$ by collision with $O_2^{\bullet-}$.

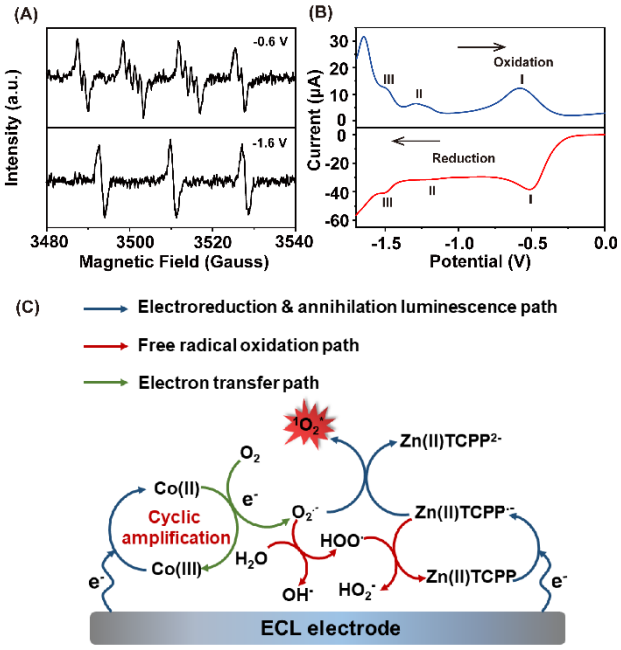

Figure 4. (A) EPR spectra of MOF **1** with DMPO and O_2 at -0.6 V (top); and with TEMP and O_2 at -1.6 V (bottom). (B) SWVs of MOF **1** in aqueous solution under O_2-saturated condition. (C) Proposed mechanism for ECL amplification of MOF **1**.

The redox processes of MOF **1** between 0 and -1.7 V were further explored by square wave voltammetry (SWV). MOF **1** undergoes three reduction processes at potential of -0.52, -1.20 and -1.51 V **(Figure 4B)**, corresponding to the generation of $HOO^{\bullet}$ and $O_2^{\bullet-}$ (0.52 V) and ZnTCPP anion radical ($ZnTCPP^{\bullet-}$ = -1.20 V, $ZnTCPP^{2-}$ = -1.51 V), respectively.[19] Considering the low starting potential (-1.4 V) required for an ECL system, the $ZnTCPP^{\bullet-}$ is an active intermediate that can collide with $O_2^{\bullet-}$ to form $^1O_2$ molecules. Due to the strong oxidizing property of $HOO^{\bullet}$ ($\varphi^{\theta}(HOO^{\bullet}/HO_2^-)$ = 0.76 V vs SHE; $\varphi(HOO^{\bullet}/HO_2^-)$ = 1.17 V when pH = 7; φ(ZnTCPP/$ZnTCPP^{\bullet-}$) = -1.00 V vs SHE), we speculate that $HOO^{\bullet}$ may help the accumulation of $ZnTCPP^{\bullet-}$ to achieve a cyclic amplification of ECL signals. Specifically, considering the efficiency of reduction reaction on the electrode is always not 100%, the unreduced $ZnTCPP^{\bullet-}$ can be oxidized to ZnTCPP by highly oxidizing $HOO^{\bullet}$, thereby changing the equilibrium constant of the reaction ($ZnTCPP + e^- \rightarrow ZnTCPP^{\bullet-}$) and increasing the amount of $ZnTCPP^{\bullet-}$ produced in this reaction. After the cyclic amplification process, the fully accumulated $ZnTCPP^{\bullet-}$ will collide with $O_2^{\bullet-}$ to generate $^1O_2$ molecules.

Based on the above results, we propose a possible ECL reaction mechanism as shown in **Figure 4C** and the following equations 1-8. Firstly, O_2 is reduced to $O_2^{\bullet-}$, while the low-spin

Co^{2+} ion is oxidized to Co^{3+} ion (Equation 1). Then, Co^{3+} is immediately electroreduced to Co^{2+} (Equation 2). The resulting $O_2^{\bullet-}$ species, on one hand, abstracts proton from water to generate $HOO^{\bullet}$ and OH^- (Equation 3), and on the other hand, collides with the $ZnTCPP^{\bullet-}$ from the electrochemical reduction of ZnTCPP (Equation 4) to produce $^1O_2$ (Equation 6).[19] In addition, the $ZnTCPP^{\bullet-}$ can also undergo an annihilation reaction with $HOO^{\bullet}$ to give ZnTCPP and HO_2^- (Equation 5). Finally, the dimerization of $^1O_2$ produces the $(^1O_2)_2^*$ species in an excited state (Equation 7), which returns to the ground state with a light-emission (Equation 8).[18, 20]

$$O_2 + Co^{2+} \rightarrow O_2^{\bullet-} + Co^{3+} \quad (1)$$

$$Co^{3+} + e^- \rightarrow Co^{2+} \quad (2)$$

$$O_2^{\bullet-} + H_2O \Leftrightarrow HOO^{\bullet} + OH^- \ (\Delta G = -0.12 \text{ eV}) \quad (3)$$

$$ZnTCPP + e^- \rightarrow ZnTCPP^{\bullet-} \quad (4)$$

$$ZnTCPP^{\bullet-} + HOO^{\bullet} \rightarrow ZnTCPP + HO_2^- \quad (5)$$

$$ZnTCPP^{\bullet-} + O_2^{\bullet-} \rightarrow ZnTCPP^{2-} + {}^1O_2 \quad (6)$$

$$2{}^1O_2 \rightarrow (^1O_2)_2^* \quad (7)$$

$$(^1O_2)_2^* \rightarrow 2{}^3O_2 + h\nu \quad (8)$$

2.3. Non-amplified detection of SARS-CoV-2

Recently, a few groups have worked to develop ECL biosensors for early diagnosis and timely detection of SARS-CoV-2.[21] However, the constant mutation of SARS-CoV-2 has caused higher viral loads with a faster spread and greater infectivity of the mutant strains. Therefore, it is urgent to develop a rapid and accurate detection method for SARS-CoV-2.

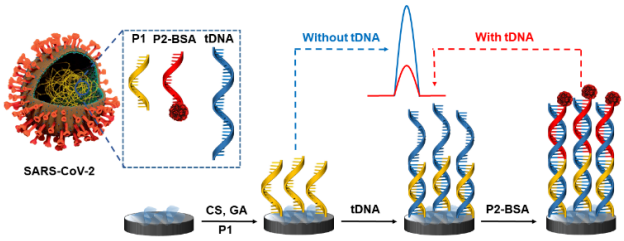

Scheme 2. ECL biosensor for the detection of RdRp-COVID DNA sequence (CS: chitosan; GA: glutaraldehyde; P1: pDNA-1; P2-BSA: bovine serum albumin (BSA)-modified pDNA-2; tDNA: RdRp gene).

Benefiting from the excellent ECL performance, the MOF **1** has been applied to the detection of RdRp gene of SARS-CoV-2 with non-amplifing mode. Specifically, MOF **1** was coated by chitosan (CS) and activated with glutaraldehyde (GA) to react with pDNA-1 (P1). The RdRp gene (tDNA) and bovine serum albumin (BSA)-modified pDNA-2 (P2-BSA) were

then ligated by complementary base pairing **(Scheme 2)**. Since BSA blocked the interfacial electron transfer from the proteins, the RdRp gene was detected by signal off mode **(Figure S18)**.

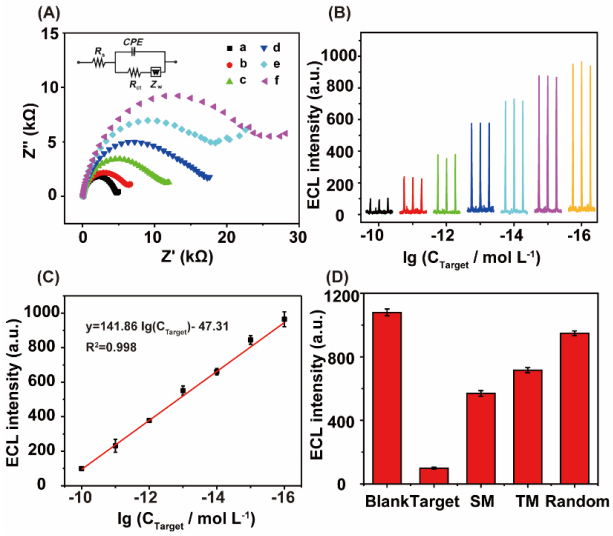

Figure 5. (A) EIS spectra for the assembly of the biosensor: (a) GCE/MOF **1**, (b) GCE/MOF **1**/CS, (c) GCE/MOF **1**/CS/pDNA-1, (d) GCE/MOF **1**/CS/pDNA-1/peptides, (e) GCE/MOF **1**/CS/pDNA-1/tDNA, (f) GCE/MOF **1**/CS/pDNA-1/tDNA/pDNA-2-BSA. (B) ECL responses of the developed biosensor towards RdRp gene with different concentrations. (C) Calibration curve for the RdRp gene detection. (D) Specificity of biosensor with various mismatched DNAs (SM: single-base mismatched, TM: three-base mismatched, random: non-complementary).

Electrochemical impedance spectroscopy (EIS) confirms the successful construction of the proposed ECL biosensor **(Figure 5A)**. In the concentration range of 100 pM to 100 aM, the ECL intensity has a linear relationship with the logarithm of the target DNA concentration **(Figure 5B and 5C)**. The linear equation is y = 141.86 lg(C_{Target}) - 47.31 with a correlation coefficient of 0.998 and the LOD calculated by the 3σ method is 30 aM, which is the lowest value reported for the ECL methods without amplification, and is also the top 3 as compared with the ECL methods with amplification (Table S1).[21] In addition, the specificity for DNA assay was proved by different mismatched and random DNAs **(Figure 5D and S20)**. Based on the high sensitivity and specificity, the ECL system of MOF **1** is expected to be a rapid and sensitive probe for the detection of SARS-CoV-2, and may be an ideal alternative to time-consuming PCR amplification methods for rapid screening SARS-CoV-2 in the initial stage of the epidemic to prevent further spread.

3. Conclusion

In summary, a novel porphyrin-based heterobimetallic 2D MOF, [(ZnTCPP)Co_2(MeIm)] (**1**), has been successfully designed and built from the electroactive [Co_2(-CO_2)$_4$] SBUs with an axially coordinated MeIm and photosensitizers (ZnTCPP) for self-enhanced ECL. By rationally regulating the amounts of MeIm, the electron transfer between the low-spin Co(II) ions and oxygen can be improved while preserving the oxygen adsorption sites, which is beneficial to the production of $O_2^{\bullet-}$. In addition, the axially coordinated MeIm can also adjust the 2D MOF **1** to a suitable distance of layers without changing the structure of layer, making the entrance of O_2 easier and exposure of ZnTCPP more sufficient. Integration of the sufficient exposure of photosensitizers ZnTCPP and the efficient generation of $O_2^{\bullet-}$ via the electroactive [Co_2(-CO_2)$_4$] SBUs in the platform synergistically enhances the ECL performance of MOF **1**. Benefiting from the excellent ECL performance, MOF **1** as a non-amplified ECL biosensor for the RdRp gene of SARS-CoV-2 shows a high sensitivity, which will have a great application potential for rapid detection of SARS-CoV-2 in the initial stage of the epidemic to prevent further spread.

4. Experimental Section/Methods

Materials and reagents: Cobalt(Ⅱ) nitrate hexahydrate ($Co(NO_3)_2{\cdot}6H_2O$, AR, 99 %), potassium chloride (KCl), sodium hydroxide (NaOH), 2-[4-(2-Hydroxyethyl)-1-piperazinyl] ethanesulfonic acid (HEPES), potassium ferricyanide ($K_3[Fe(CN)_6]$), potassium ferrocyanide ($K_4[Fe(CN)_6]$), ethanol and methanol were purchased from Aladdin (Shanghai, China). Tetraoctylammonium bromide (TOAB) was obtained from Alfa Aesar Chemicals Co. Ltd. (Shanghai, China). 2-methylimidazole (MeIm, AR, 99%) was bought from Maclin (Shanghai, China). Zinc(II) tetrakis(4-carboxyphenyl)porphine (ZnTCPP) was commercially available from J & K Chemical Ltd (Shanghai, China). Ultrapure water obtained from a Millipore water purification system (≥18 MΩ, Milli-Q, Millipore) was used for the whole experiment. ECL measurements were conducted in 10 mM HEPES buffer solution at pH 7.0 containing 0.1 M KCl as the electrolyte.

Characterization: The morphologies of the synthesized hybrid materials were investigated by using FEI Quanta250 Field Emission Scanning Electron Microscope (FESEM). Fourier-transformation infrared (FT-IR) spectra were recorded with an IR-Prestige-21 FT-IR spectrometer (Shimadzu Co., Japan). Powder X-ray diffraction patterns (PXRD) analysis was carried out on a Bruker D8-Focus Bragg-Brentano X-ray Powder diffractometer equipped

with a Cu sealed tube (λ = 1.54178 Å) at room temperature. X-ray photoelectron spectroscopy (XPS) was performed by K-Alpha X-ray photoelectron spectroscopy (PHI Quantera II ESCA System). The fluorescence spectra were recorded on a fluorescence spectrophotometer (Edinburgh Analytical Instruments, FLS920). Cyclic voltammetries (CVs) were measured using a CHI 660D electrochemical workstation (CHI Co., USA). ECL measurements were carried out on a MPI-E multifunctional electrochemical and chemiluminescent analytical system (Xi'an Remex Analytical Instrument Co., Ltd, China). Electrochemical impedance spectroscopy (EIS) measurements were conducted using an Autolab PGSTAT30 (Eco Chemie) controlled by NOVA 1.10 software. All electrochemical studies were carried out with a conventional three electrode system. A Pt wire electrode and an Ag/AgCl electrode were used as counter and reference electrodes, respectively. Modified glassy carbon electrodes (GCE, 5 mm in diameter) were used as working electrodes.

Synthesis of 2D MOF 1: MeIm (3.3 mg, 0.04 mmol, 2 mL methanol) and ZnTCPP (8.5 mg, 0.01 mmol, 10 mL methanol) solution were mixed under stirring. Then the solution of $Co(NO_3)_2 \cdot 6H_2O$ (5.8 mg, 0.02 mmol) in 3 mL methanol was added into the above mixed solution. The resulting mixture was stirred vigorously at room temperature for 24 h and the precipitated green-purple powder was then collected by centrifugation (4000 rpm, 10 min), washed with methanol (3 × 10 mL), and dried in vacuum at 60°C for 12 h to give the MOF **1** material. Yield: 9.9 mg, 56.2%

To monitor the MeIm axial coordination number, based on the above protocol, the addition amount of MeIm was changed to 0.05 mmol (4.1 mg) and 0.06 mmol (5.0 mg) to synthesize MOF **1** with different amounts of MeIm.

Synthesis of MOF 2: A solution of $Co(NO_3)_2 \cdot 6H_2O$ (5.8 mg, 0.02 mmol) in 3 mL methanol and a solution of ZnTCPP (8.5 mg, 0.01 mmol) in 10 mL methanol were mixed with stirring. The resulting mixture was stirred vigorously at 60°C for 24 h and the precipitated green-purple powder was then collected by centrifugation (4000 rpm, 10 min), washed with methanol (3 × 10 mL), and dried in vacuum at 60°C for 12 h to give the MOF **2** material.

Synthesis of [(ZnTCPP)Zn_2(MeIm)]: MeIm (4.1 mg, 0.05 mmol, 2 mL methanol) and TCPP (8.5 mg, 0.01 mmol, 10 mL methanol) solution were mixed under stirring. Then the solution of $Zn(NO_3)_2 \cdot 6H_2O$ (8.9 mg, 0.03 mmol) in 3 mL methanol was added into the above mixed solution. The resulting mixture was stirred vigorously at room temperature for 24 h and the precipitated green-purple powder was then collected by centrifugation (4000 rpm, 10 min), washed with methanol (3 × 10 mL), and dried in vacuum at 60°C for 12 h to give the [(ZnTCPP)Zn_2(MeIm)] material.

Synthesis of [(CoTCPP)Co_2(MeIm)]: MeIm (4.1 mg, 0.05 mmol, 2 mL methanol) and TCPP (8.5 mg, 0.01 mmol, 10 mL methanol) solution were mixed under stirring. Then the solution of $Co(NO_3)_2 \cdot 6H_2O$ (8.7 mg, 0.03 mmol) in 3 mL methanol was added into the above mixed solution. The resulting mixture was stirred vigorously at room temperature for 24 h and the precipitated green-purple powder was then collected by centrifugation (4000 rpm, 10 min), washed with methanol (3 × 10 mL), and dried in vacuum at 60°C for 12 h to give the [(CoTCPP)Co_2(MeIm)] material.

Preparation of BSA modified pDNA-2 (P2-BSA): Solution A consisted of 200 μL pDNA-2 (1×10^{-6} mol L^{-1}) and 100 μL 12.5% glutaraldehyde (GA), which was incubated at 37 °C for 1 h with shaking. Then, 100 μL 1% BSA was added to solution A, and the mixture was shaken at 37 °C for 2 h. Finally, the resulting solution was washed with ultrapure water (3 × 4 mL) through an ultrafiltration tube (MWCO = 30 KD) to remove unreacted pDNA-2 and glutaraldehyde. The resulting pDNA-2 for the RdRp gene with BSA modified was named P2-BSA.

Fabrication of the ECL biosensor: The GCE (d=5 mm) was polished carefully with 0.3 and 0.05 μm of Al_2O_3 powder and sonicated sequentially in ethanol and rinsed by deionized water for further use. 5 μL MOF **1** (1 mg mL^{-1} in aqueous solution) was spread on the GCE and coated with 10 μL chitosan (0.1% w/w in 2% acetic acid solution) and dried at room temperature to obtain the CS/MOF **1**/GCE. Subsequently, 20 μL GA (12.5% w/w in water) was dropped onto the CS/MOF **1**/GCE and incubated at 37 °C for 1 h. After the reaction, the electrodes were washed with ultrapure water (3 × 2 mL), and 20 μL pDNA-1 (1×10^{-6} mol L^{-1}) was then covered onto the above mentioned modified GCE and left for 2 h at 37 °C. After that, 20 μL peptides solution (1% w/w in water) was distributed onto the surface to block the non-specific binding sites. After being washed thoroughly with ultrapure water (3 × 2 mL), 20 μL of the tDNA was dropped onto the surface of the electrode and incubated at 37 °C for 2 h. After rinsing thoroughly with ultrapure water (3 × 2 mL), 20 μL P2-BSA was added to the electrode and incubated at 37 °C for 2 h. Finally, the electrode would generate ECL signal in the O_2-saturated aqueous electrolyte solution and gave the quantitative criteria for the proposed DNA assay.

Calculation Method: All density function theory (DFT) calculations were performed based on the projector-augmented-wave method as implemented in the Vienna Ab initio simulation package (VASP). The Blöchl's all-electron-like projector augmented plane wave (PAW) method was used to describe the interactions between ion cores and valence electrons. The electronic exchange-correlation potential was treated within the functional of Perdew-Burke-

Ernzerhof (PBE) function for generalized gradient approximation (GGA). The plane-wave cutoff was set to 400 eV and the convergence threshold was set as 1×10^{-3} eV in energy and 0.02 eVÅ^{-1} in force. The Monkhorst-Pack k-point was set with 3 × 3 × 1 grid meshes for structure optimization. The DFT-D3 method is adopted to describe the weak van der Waals (vdW) interactions between the adsorbate and the substrate. The adsorption energy (E_{ads}) of O_2 is calculated by the following formula:

$E_{ads}=E_{sa}-E_{ad}-E_s$

where E_{sa}, E_{ad} and E_s represent the total energies of the adsorbate plus substrate system, isolated adsorbate and pure substrate, respectively.

In addition, HOMO, LUMO and Mulliken charge distributions are calculated by Dmol^3 module in the Materials studio program based on the GGA-PBE method.

Supporting Information

Supporting Information is available from the Wiley Online Library or from the author.

Acknowledgements

This research was supported by the National Natural Science Foundation of China (No. 22274075) and "Overseas Academic Partnership Program" of Nanjing University of Technology (2019). The authors wish also to acknowledge the support from the Sino-French international research network "New nanostructured materials and biomaterials for renewable electrical energy sources".

Received: ((will be filled in by the editorial staff))

Revised: ((will be filled in by the editorial staff))

Published online: ((will be filled in by the editorial staff))

References

[1] a) W. Guo, H. Ding, C. Gu, Y. Liu, X. Jiang, B. Su, Y. Shao, *J. Am. Chem. Soc.* **2018**, *140*, 15904; b) W. Guo, H. Ding, P. Zhou, Y. Wang, B. Su, *Angew. Chem. Int. Ed.* **2020**, *59*, 6745.

[2] a) D. Zhu, Y. Zhang, S. Bao, N. Wang, S. Yu, R. Luo, J. Ma, H. Ju, J. Lei, *J. Am. Chem. Soc.* **2021**, *143*, 3049; b) Y. Wang, G. Zhao, H. Chi, S. Yang, Q. Niu, D. Wu, W. Cao, T. Li, H. Ma, Q. Wei, *J. Am. Chem. Soc.* **2021**, *143*, 504; c) X. Tan, B. Zhang, G. Zou, *J. Am. Chem. Soc.* **2017**, *139*, 8772.

[3] a) T. Wang, D. Wang, J. W. Padelford, J. Jiang, G. Wang, *J. Am. Chem. Soc.* **2016**, *138*, 6380; b) S. Carrara, F. Arcudi, M. Prato, L. De Cola, *Angew. Chem. Int. Ed.* **2017**, *56*, 4757.

[4] a) Y. Zhou, M. Chen, Y. Zhuo, Y. Chai, W. Xu, R. Yuan, *Anal. Chem.* **2017**, *89*, 6787; b) Y. Zhou, Y. Chai, R. Yuan, *Anal. Chem.* **2019**, *91*, 14618; c) Irkham, A. Fiorani, G. Valenti, N. Kamoshida, F. Paolucci, Y. Einaga, *J. Am. Chem. Soc.* **2020**, *142*, 1518.

[5] a) K. Yu, T. Wei, Z. Li, J. Li, Z. Wang, Z. Dai, *J. Am. Chem. Soc.* **2020**, *142*, 21267; b) J. Jia, L. Gutierrez-Arzaluz, O. Shekhah, N. Alsadun, J. Czaban-Jozwiak, S. Zhou, O. M. Bakr, O. F. Mohammed, M. Eddaoudi, *J. Am. Chem. Soc.* **2020**, *142*, 8580; c) S. Liu, H. Chen, H. Lv, Q. P. Qin, L. Fan, X. Zhang, *Mater. Today Chem.* **2022**, *24*, 100984; d) H. Chen, T. Zhang, S. Liu, H. Lv, L. Fan, X. Zhang, *Inorg. Chem* **2022**, *61*, 11949.

[6] E.-Y. Choi, C. A. Wray, C. Hu, W. Choe, *CrystEngComm* **2000**, *11*, 553.

[7] H. Abu Ali, A. Abu Shamma, S. Kamel, *J. Mol. Struct.* **2017**, *1142*, 40.

[8] D. Kiani, J. Baltrusaitis, *Catal. Today* **2021**, *365*, 24.

[9] A. Wang, L. Long, W. Zhao, Y. Song, M. G. Humphrey, M. P. Cifuentes, X. Wu, Y. Fu, D. Zhang, X. Li, C. Zhang, *Carbon* **2013**, *53*, 327.

[10] C. Guo, Y. Zhang, L. Zhang, Y. Guo, N. Akram, J. Wang, *ACS Appl. Nano Mater.* **2018**, *1*, 5289.

[11] X. Wang, Z. Yang, W. Si, X. Shen, X. Li, R. Li, Q. Lv, N. Wang, C. Huang, *Carbon* **2019**, *147*, 9.

[12] L.-H. Xu, S.-L. Zhang, S.-Y. Guo, X.-J. Zhang, S. Cosnier, R. S. Marks, W.-J. Wang, H.-B. Zeng, D. Shan, *J. Catal.* **2020**, *387*, 129.

[13] M. A. Peck, M. A. Langell, *Chem. Mater.* **2012**, *24*, 4483.

[14] J. Zhao, Q. Peng, Z. Wang, W. Xu, H. Xiao, Q. Wu, H. L. Sun, F. Ma, J. Zhao, C. J. Sun, J. Zhao, J. Li, *Nat. Commun.* **2019**, *10*, 2303.

[15] I. Liberman, R. Shimoni, R. Ifraemov, I. Rozenberg, C. Singh, I. Hod, *J. Am. Chem. Soc.* **2020**, *142*, 1933.

[16] W. C. Huo, X. a. Dong, J. Y. Li, M. Liu, X. Y. Liu, Y. X. Zhang, F. Dong, *Chem. Eng. J.* **2019**, *361*, 129.

[17] W. Gu, H. Wang, L. Jiao, Y. Wu, Y. Chen, L. Hu, J. Gong, D. Du, C. Zhu, *Angew. Chem. Int. Ed.* **2020**, *59*, 3534.

[18] G. Y. Zhang, C. Cai, S. Cosnier, H. B. Zeng, X. J. Zhang, D. Shan, *Nanoscale* **2016**, *8*, 11649.

[19] G. Pu, Z. Yang, Y. Wu, Z. Wang, Y. Deng, Y. Gao, Z. Zhang, X. Lu, *Anal. Chem.* **2019**, *91*, 2319.

[20] S. Senthil Kumar, A. J. Bard, *Anal. Chem.* **2013**, *85*, 292.

[21] a) Z. Fan, B. Yao, Y. Ding, D. Xu, J. Zhao, K. Zhang, *Chem. Eng. J.* **2022**, *427*, 131686; b) K. Zhang, Z. Fan, Y. Huang, Y. Ding, M. Xie, *Talanta* **2022**, *236*, 122868.

Yi-Xuan Li, Jing Li, Dunru Zhu*, Ju-Zheng Wang, Guo-Fang Shu, Junji Li, Sheng-Li Zhang*, Xue-Ji Zhang, Serge Cosnier, Hai-Bo Zeng, Dan Shan*

2D Zn-porphyrin-based Co(II)-MOF with 2-Methylimidazole Sitting Axially on the Paddle-wheel Units: An Efficient Electrochemiluminescence Bioassay for SARS-CoV-2

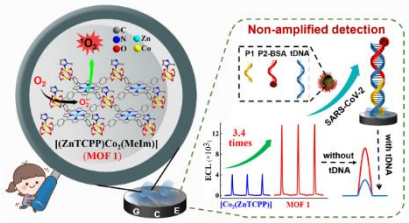

A novel porphyrin-based heterobimetallic 2D MOF, [(ZnTCPP)Co_2(MeIm)] **(1)** has been constructed to act as an excellent electrochemiluminescence probe for rapid non-amplified detection of SARS-CoV-2.

Supporting Information

2D Zn-porphyrin-based Co(II)-MOF with 2-Methylimidazole Sitting Axially on the Paddle-wheel Units: An Efficient Electrochemiluminescence Bioassay for SARS-CoV-2

Yi-Xuan Li, Jing Li, Dunru Zhu, Ju-Zheng Wang, Guo-Fang Shu, Junji Li, Sheng-Li Zhang*, Xue-Ji Zhang, Serge Cosnier, Hai-Bo Zeng, Dan Shan**

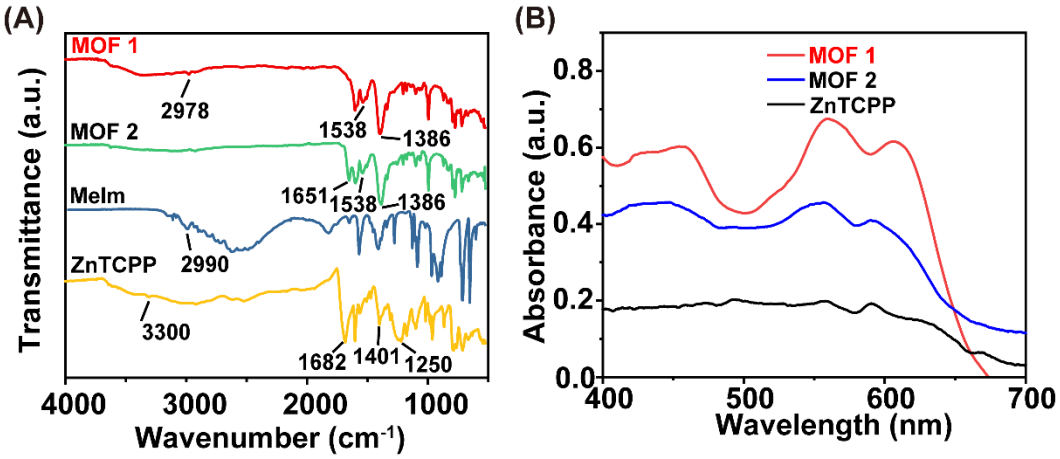

Figure S1 (A) FT-IR spectra of ZnTCPP, MeIm, MOFs **1** and **2**. **(B)** UV–vis DR spectra of ZnTCPP, MOFs **1** and **2**.

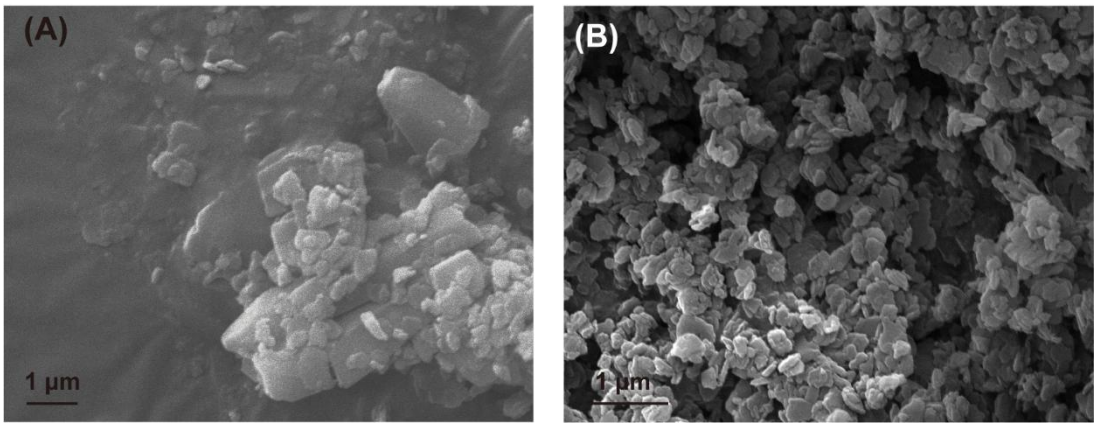

Figure S2 SEM image of **(A)** MOF **2** and **(B)** MOF **1**.

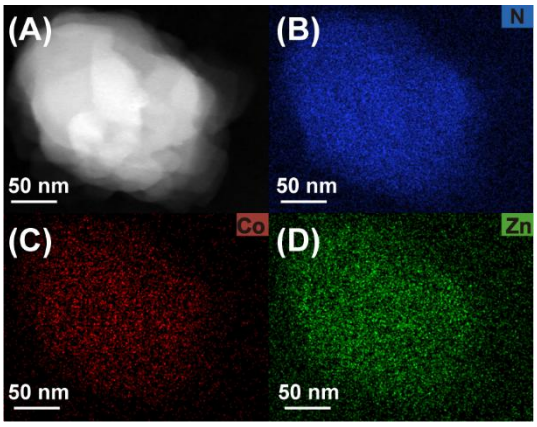

Figure S3 (A) HAADF-STEM mapping profiles of **(B)** N, **(C)** Co and **(D)** Zn of MOF **1**.

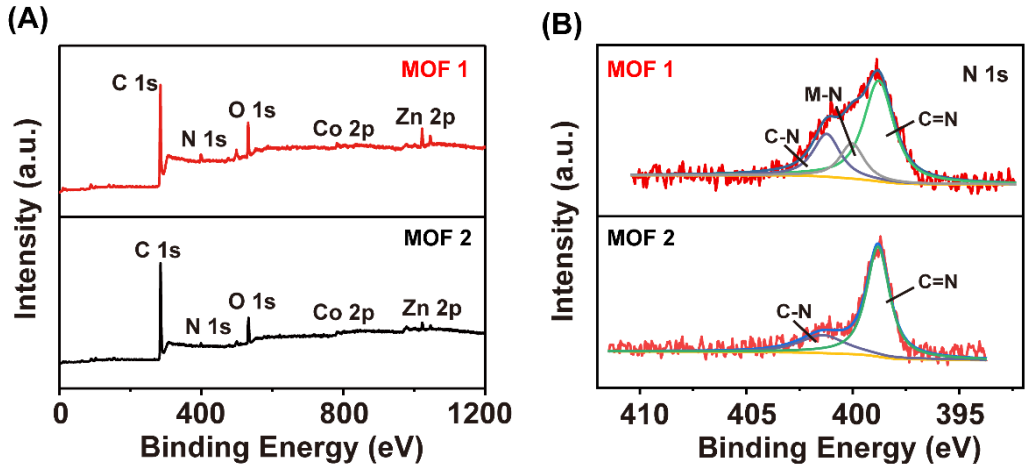

Figure S4 XPS survey scan **(A)** and high-resolution XPS response of N 1s **(B)** of MOFs **1** and **2**.

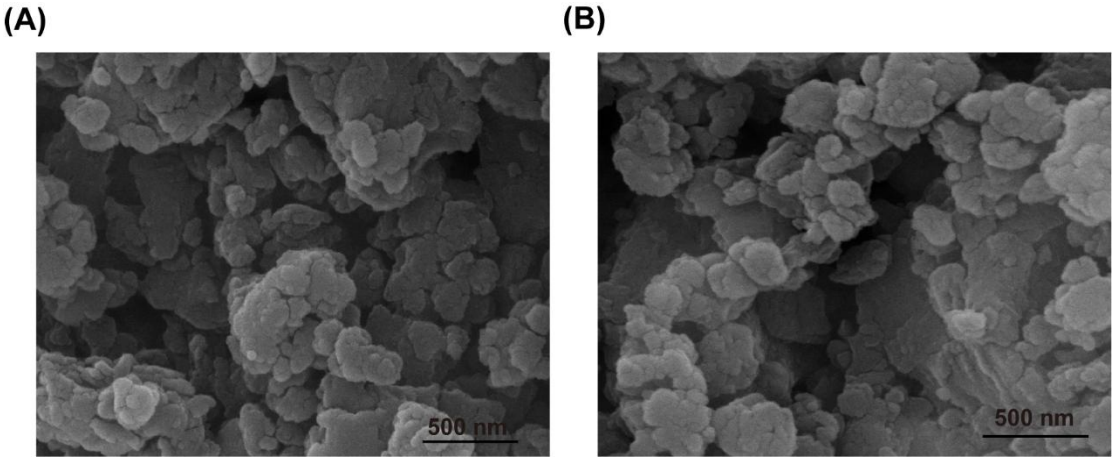

Figure S5 SEM image of MOF **1** with **(A)** ZnTCPP: MeIm=1:5; **(B)** ZnTCPP: MeIm=1:6.

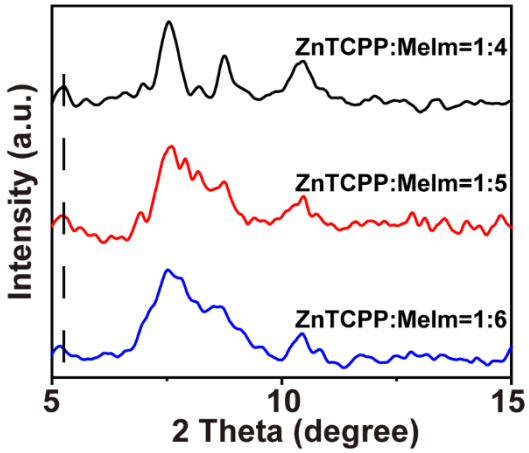

Figure S6 XRD patterns of MOF **1** with different concentrations of MeIm.

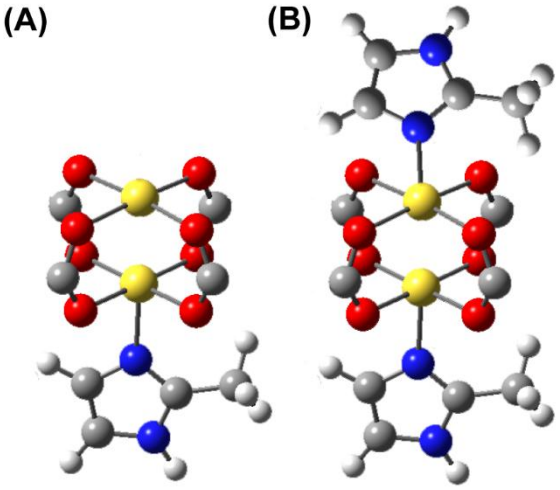

Figure S7 Paddle wheel units of MOF **1** with **(A)** ZnTCPP: MeIm = 1:5; **(B)** ZnTCPP: MeIm = 1:6.

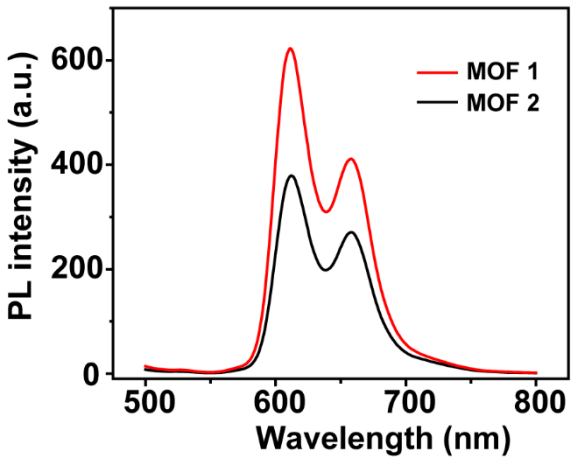

Figure S8 PL intensity of MOFs **1** and **2**.

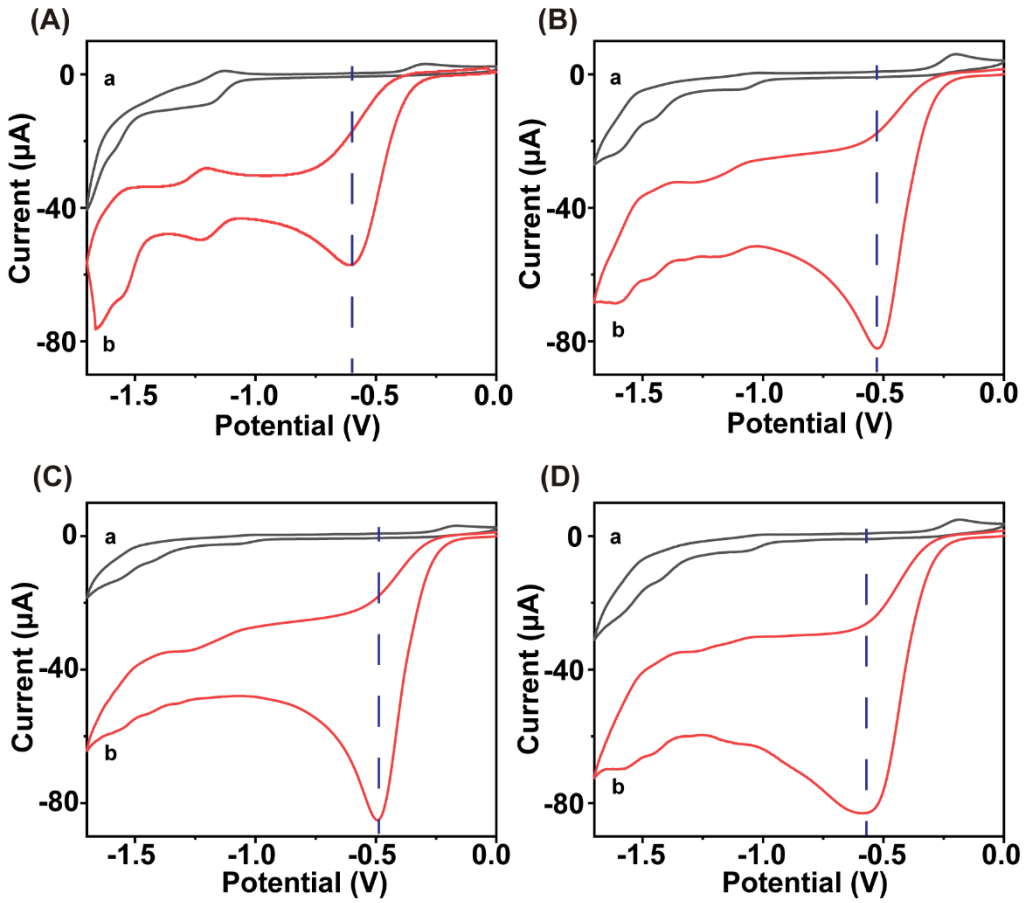

Figure S9 CVs of **(A)** MOF **2** and **(B-D)** MOF **1** in aqueous solution under N_2 (a) and O_2-saturated condition (b). **(B)** ZnTCPP: MeIm = 1:4, **(C)** ZnTCPP: MeIm = 1:5, **(D)** ZnTCPP: MeIm = 1:6.

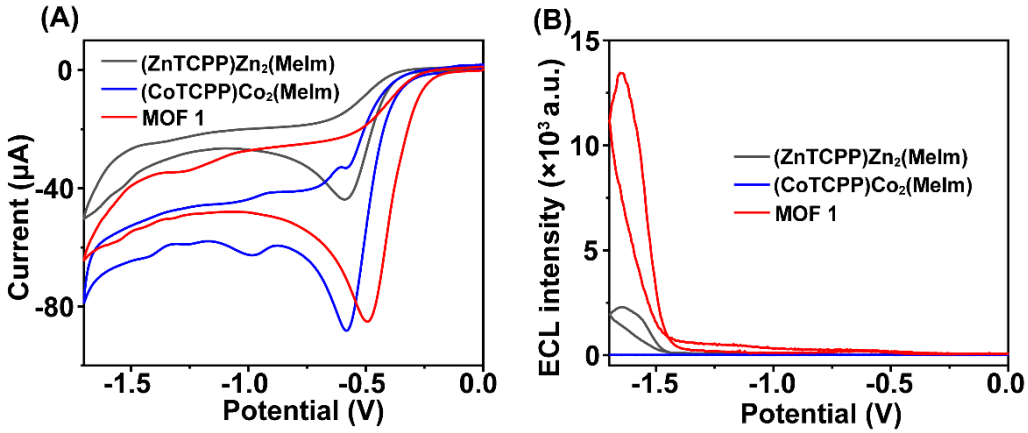

Figure S10 (A) Cyclic voltammograms of [(ZnTCPP)Zn_2(MeIm)], [(CoTCPP)Co_2(MeIm)] and MOF **1** in 10 mmol L^{-1} (pH 7.4) HEPES containing 0.3 mol L^{-1} O_2-saturated KCl solution vs Ag/AgCl reference potential. **(B)** ECL-potential curves of [(ZnTCPP)Zn_2(MeIm)], [(CoTCPP)Co_2(MeIm)] and MOF **1** in aqueous solution under O_2-saturated condition.

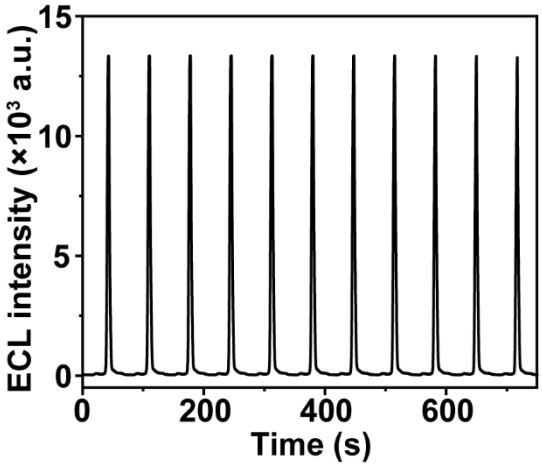

Figure S11 ECL responses of MOF **1** recorded in aqueous solution during a continuous potential scan between −1.7 and 0 V under O_2-saturated condition.

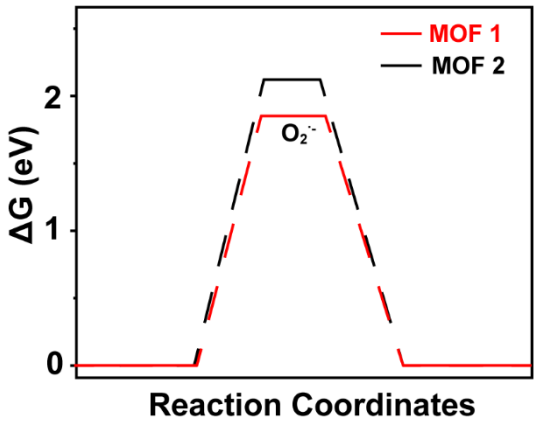

Figure S12 Free-energy diagram of O_2 desorption on active metal sites in MOFs **1** and **2**.

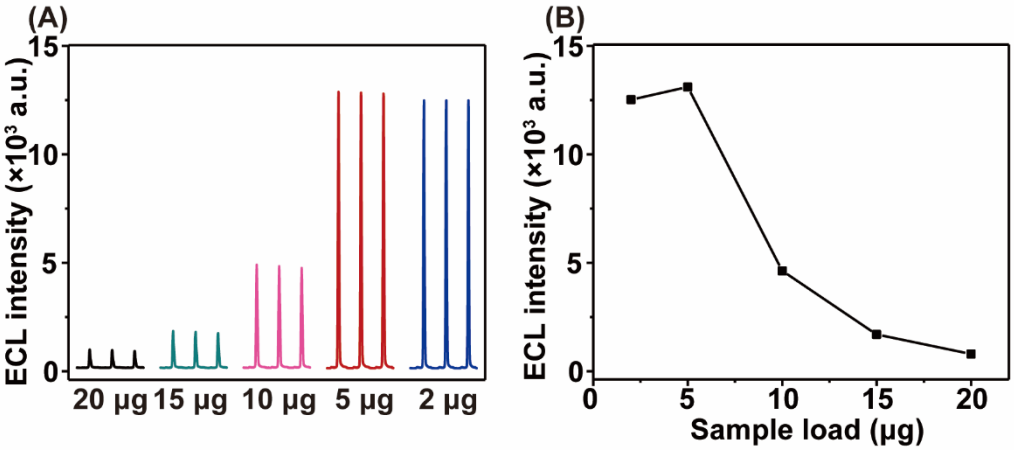

Figure S13 ECL intensity of MOF **1 (A)** during a continuous potential scan and **(B)** at final stability over various sample load.

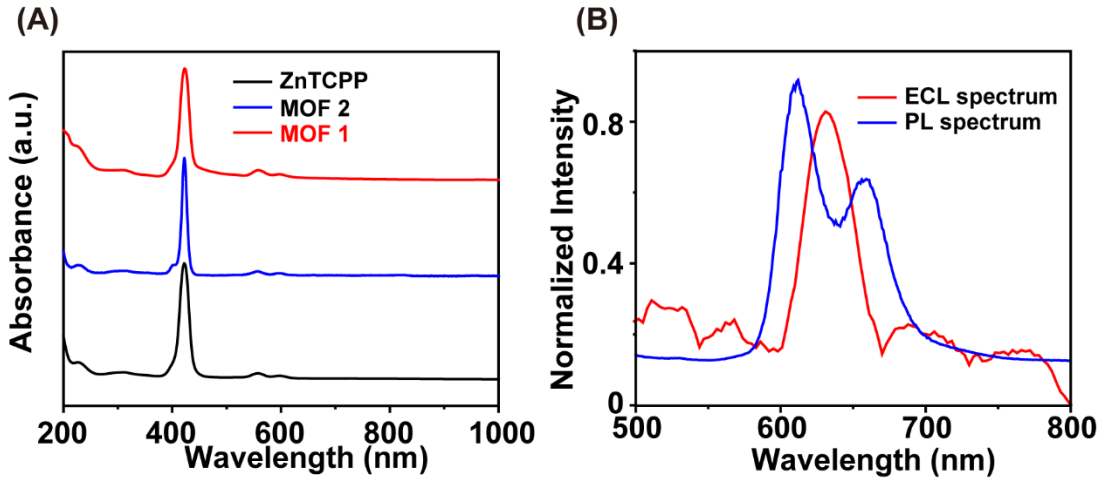

Figure S14 (A) UV−vis absorption of ZnTCPP, MOFs **1** and **2**. **(B)** ECL and PL spectra (λ_{em} = 420 nm) of MOF **1**.

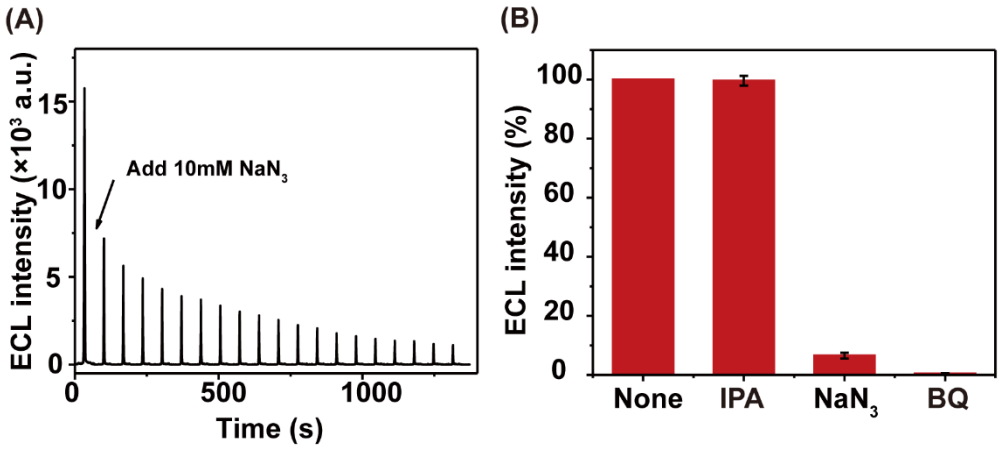

Figure S15 (A) ECL intensity variation with added 10 mM sodium azide (NaN_3) as singlet oxygen scavengers. **(B)** Statistic graph of ECL intensity after addition of 10 mM different quenchers (IPA: quencher for •OH, NaN_3: quencher for $^1O_2$, BQ: quencher for $O_2^{\bullet-}$).

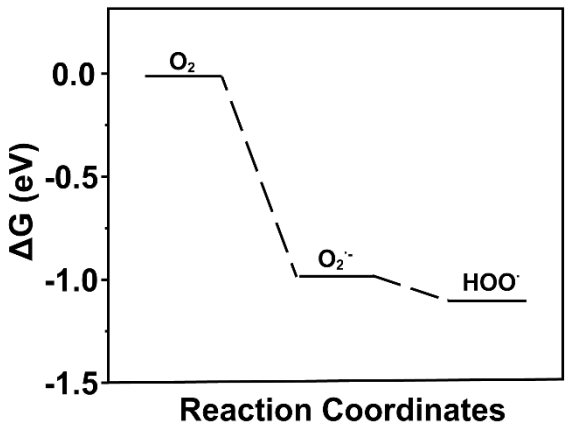

Figure S16 The free energy profile for the oxygen reduction to $O_2^{\bullet-}$ and $HOO^{\bullet}$ pathway over MOF **1**.

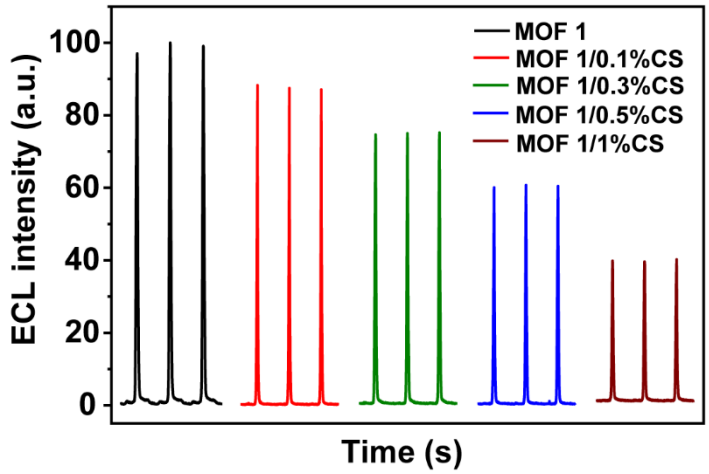

Figure S17 ECL responses of different concentration of chitosan-coated MOF **1.**

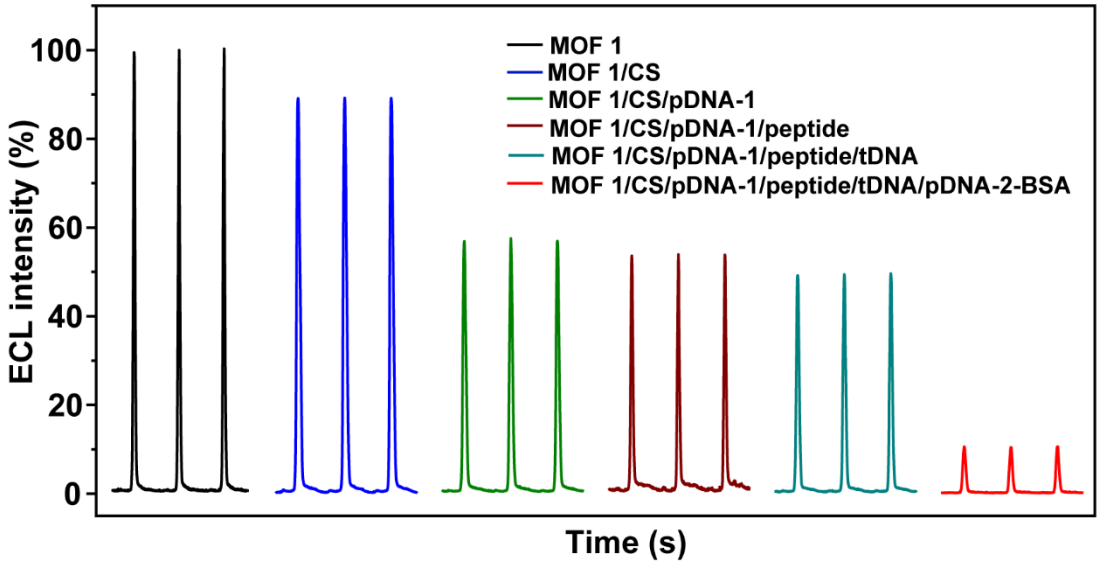

Figure S18 ECL responses of the assembly of the biosensor.

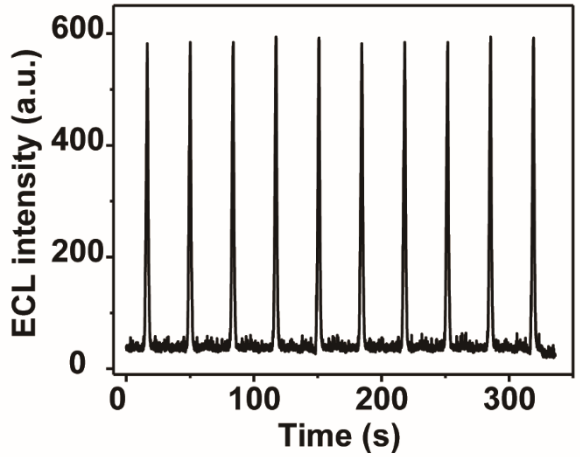

Figure S19 ECL-time response of the biosensor at RdRp gene concentration of 100 fM under continuous potential scan with a scan rate of 100 mV s^{-1} in O_2-saturated pH 7.4 HEPES solution.

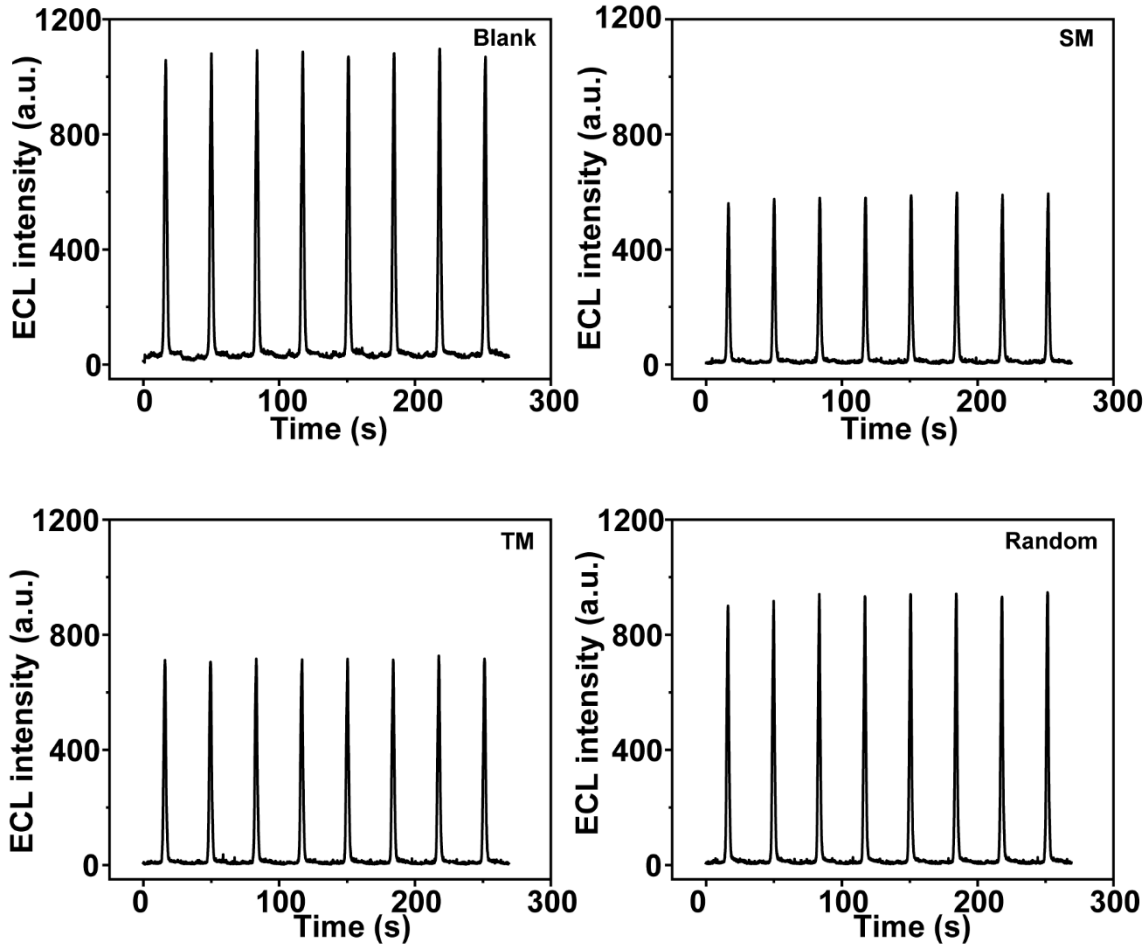

Figure S20 ECL-time response of the biosensor with different DNA sequences (SM: single-base mismatched, TM: three-base mismatched, random: non-complementary) under continuous potential scan with a scan rate of 100 mV s^{-1} in O_2-saturated pH 7.4 HEPES solution.

Table S1. Comparisons of our methods with other DNA detecting method reported previously. Incubation time has been converted according to commercial detection (DNA complementary pairing: 5 min, enzyme digestion: 5 min, amplification time is based on the report)

Method	Materials	LOD	Time	Reference
RT-qPCR	/	1.3×10^{-18} M	3-4 h	[1]
Colorimetric	AuNPs	4.3×10^{-8} M	10 min	[2]
Electrochemistry	Au-DNA	1×10^{-14} M	10 min	[3]
ECL (with amplification)	Au-gC_3N_4&PEI-Ru@Ti_3C_2@AuNPs	7.8×10^{-18} M	60 min	[4]
ECL (with amplification)	PEI-Ru@Ti_3C_2 @AuNPs	1.3×10^{-17} M	70 min	[5]
ECL (with amplification)	GOAu-Ru	3.3×10^{-17} M	2 h	[6]
ECL (without amplification)	Ti_3C_2/PEI-Ru(dcbpy)$_3^{2+}$@Au	6.8×10^{-13} M	10 min	[7]
ECL (without amplification)	AuNM&CDs	5.1×10^{-16} M	5 min	[8]
ECL (without amplification)	MOF **1**	**3×10^{-17} M**	**5 min**	**This work**

Table S2 Oligonucleotides sequences involved in the experiments.

note	sequence (5'-3')
pDNA-1	CTGATGAGGTTCCACCTG-$(CH_2)_6$-NH_2
pDNA-2	NH_2-$(CH_2)_6$-GCAGTTGTGGCATCTC
tDNA (RdRp gene)	CAGGTGGAACCTCATCAGGAGATGCCACAACTGC
Single-base mismatched	CAGGTGTAACCTCATCAGGAGATGCCACAACTGC
Three-base mismatched	CAGGTGTAACCTCATCAGGAAATGCCACAGCTGC
Non-complementary	ACTTACCTTTGCTCATTGACGTGGCTATGAGCTA

References

[1] T. Ji, Z. Liu, G. Wang, X. Guo, S. Akbar Khan, C. Lai, H. Chen, S. Huang, S. Xia, B. Chen, H. Jia, Y. Chen, Q. Zhou, *Biosens. Bioelectron.* **2020**, *166*, 112455.

[2] P. Moitra, M. Alafeef, K. Dighe, M. B. Frieman, D. Pan, *ACS Nano* **2020**, *14*, 7617.

[3] Y. Wan, P. Wang, Y. Su, L. Wang, D. Pan, A. Aldalbahi, S. Yang, X. Zuo, *ACS Appl. Mater. Interfaces* **2015**, *7*, 25618.

[4] Z. Fan, B. Yao, Y. Ding, D. Xu, J. Zhao, K. Zhang, *Chem. Eng. J.* **2022**, *427*, 131686.

[5] K. Zhang, Z. Fan, Y. Huang, Y. Ding, M. Xie, *Talanta* **2022**, *236*, 122868.

[6] K. Zhang, Z. Fan, Y. Ding, S. Zhu, M. Xie, N. Hao, Environ. *Sci. Nano* **2022**, *9*, 162.

[7] Z. Fan, M. Xie, J. Pan, K. Zhang, Environ. *Chem. Lett.* **2022**, *20*, 2227.

[8] L. Gutierrez-Galvez, R. Del Cano, I. Menendez-Luque, D. Garcia-Nieto, M. Rodriguez-Pena, M. Luna, T. Pineda, F. Pariente, T. Garcia-Mendiola, E. Lorenzo, *Talanta* **2022**, *240*, 123203.